Environmental Science & Technology

pubs.acs.org/est

Article

High-Precision Microscale Particulate Matter Prediction in Diverse Environments Using a Long Short-Term Memory Neural Network and Street View Imagery

Xiansheng Liu,* Xun Zhang,* Rui Wang, Ying Liu, Hadiatullah Hadiatullah, Yanning Xu, Tao Wang, Jan Bendl, Thomas Adam, Jürgen Schnelle-Kreis, and Xavier Querol

Cite This: *Environ. Sci. Technol.* 2024, 58, 3869−3882

Read Online

ACCESS | Metrics & More | Article Recommendations | Supporting Information

ABSTRACT: In this study, we propose a novel long short-term memory (LSTM) neural network model that leverages color features (HSV: hue, saturation, value) extracted from street images to estimate air quality with particulate matter (PM) in four typical European environments: urban, suburban, villages, and the harbor. To evaluate its performance, we utilize concentration data for eight parameters of ambient PM ($PM_{1.0}$, $PM_{2.5}$, and PM_{10}, particle number concentration, lung-deposited surface area, equivalent mass concentrations of ultraviolet PM, black carbon, and brown carbon) collected from a mobile monitoring platform during the nonheating season in downtown Augsburg, Germany, along with synchronized street view images. Experimental comparisons were conducted between the LSTM model and other deep learning models (recurrent neural network and gated recurrent unit). The results clearly demonstrate a better performance of the LSTM model compared with other statistically based models. The LSTM-HSV model achieved impressive interpretability rates above 80%, for the eight PM metrics mentioned above, indicating the expected performance of the proposed model. Moreover, the successful application of the LSTM-HSV model in other seasons of Augsburg city and various environments (suburbs, villages, and harbor cities) demonstrates its satisfactory generalization capabilities in both temporal and spatial dimensions. The successful application of the LSTM-HSV model underscores its potential as a versatile tool for the estimation of air pollution after presampling of the studied area, with broad implications for urban planning and public health initiatives.

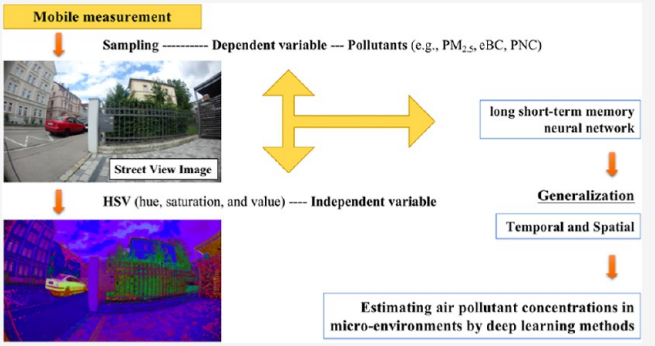

KEYWORDS: *PM metrics, deep learning, LSTM, exposure assessment models, air quality*

1. INTRODUCTION

A large number of studies have confirmed the impact of urban air pollutants on the environment,[1] including human health.[2] Accordingly, it is very important to carry out continuous monitoring of major urban outdoor pollutants. The current research work on the mass concentration of air pollutants is mostly limited to short term and microclimate conditions.[3] Even if continuous monitoring with high time resolution is established, it is mostly at a single monitoring point.[4] For urban areas, there is a lack of comprehensive, systematic, and effective multipoint data for research. At the same time, due to the diverse and variable pollution sources of atmospheric particulate matter (PM) metrics such as PM and black carbon (BC), there remain numerous unresolved issues concerning their generation mechanisms,[5,6] and their mass concentrations might be highly heterogeneous on the spatial scale and time.[7] Consequently, the task of attaining a comprehensive forecast of pollutant levels in diverse urban microenvironments remains a substantial and persistent challenge.

Previous research studies on environmental prediction methods mostly used mathematical model methods to make predictions. The developed method in the pattern of urban air pollutants is mainly based on the prediction of their mass concentrations. Typical models include the case-based reasoning system, the lazy learning method,[8] σ-fuzzy lattice neurocomputing model,[9] land use regression (LUR) models,[10] some other classical models (e.g., box-type, multisource diffusion, Gaussian diffusion, line and area source diffusion, and total suspended microparticle diffusion).[11,12] In general, these prediction methods mainly analyze the relationship between atmospheric pollutant concentration and its related

Received: August 10, 2023
Revised: December 18, 2023
Accepted: December 28, 2023
Published: February 14, 2024

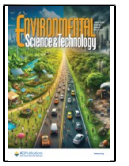

https://doi.org/10.1021/acs.est.3c06511
Environ. Sci. Technol. 2024, 58, 3869−3882

influencing factors, including population and traffic density, industrial fuel consumption, land use, and other related factors. However, these approaches involving the regression of categorical variables can produce ambiguous results because some data are ignored. For instance, a significant amount of data is required when using LUR models, and there is limited capture of the features in detail, resulting in limited accuracy in explaining pollutant concentrations.[13] Furthermore, some traditional models may struggle to capture the complex interplay of dynamic environmental factors. For instance, Gaussian dispersion models, while widely used, assume steady-state conditions and uniform meteorological conditions,[14] which may not always reflect the real-world variability and turbulence in urban environments. Moreover, reliance on historical data and fixed parameters in traditional models may hinder their adaptability to rapidly changing urban landscapes. Factors such as rapid urbanization, shifts in transportation patterns, and evolving industrial activities can challenge the accuracy and applicability of these models over time.

Relative to mathematical model methods, deep learning methods offer a new perspective on the prediction of atmospheric pollutant concentrations. It is motivated by creating and modeling the brain's analytic learning neural networks, mimicking the mechanisms of the human brain to interpret data. Bai and Shen (2019) used the long short-term memory (LSTM) model to predict $PM_{2.5}$ concentrations and obtained better results.[15] Menares et al. (2021) employed both a deep feedforward neural network (DFFNN) and LSTM models to forecast the $PM_{2.5}$ concentration value, with the LSTM model outperforming the DFFNN model and achieving the highest accuracy of 0.87.[4] While these models enhance the precision of predictions to varying extents, they face a common limitation: as the length of the time series grows, data points that are further away from the present information become increasingly disregarded.[16] This can lead to a loss of valuable information that may be crucial for accurate forecasting. However, street view images obtained within urban street canyons provide a human-centric perspective of the built environment, offering a promising avenue to access information about the surrounding environment. For instance, Hankey and Marshall (2015) studied the regression models of video-derived traffic counts and particle concentrations.[17] They used the counts of each vehicle type (i.e., passenger cars, trucks, and buses) as independent variables in the regression model to estimate the PM concentration. Messier et al. (2018) mapped spatial air quality patterns using an unusually rich data set of repeated mobile air quality measurements collected with specially equipped Google Street View cars.[18] Furthermore, deep learning-based computer vision algorithms have achieved notable advancements, gaining broad recognition and triumph across diverse domains owing to their remarkable ability for autonomous learning and representation of image features.[19−23] As of now, image-based pollution models have been essentially developed in various regions worldwide.[24−29] The majority of research techniques employ image segmentation to quantify urban streetscapes.[7,19]

In a prior study, we created a model based on streetscape images to estimate urban BC levels. The model was effectively utilized with street images to evaluate air pollution concentrations. However, the model was able to account for only 68% of neighborhood-scale BC predictions and had constraints in predicting exposure to other pollutants, and the model generalization in other sites need further improvement.[7] Furthermore, the previous study necessitates sophisticated segmentation techniques for the images, as it involves the extraction and classification of street view images.[7] Consequently, there is an urgent demand for a more straightforward approach for establishing the relationship between street images and pollutant levels.

In this study, we address the estimation of several mostly typical monitoring PM metrics, including PM_X ($PM_{1.0}$, $PM_{2.5}$, and PM_{10}), ultraviolet PM (UVPM), BC, brown carbon (BrC), particle number concentration (PNC), and lung-deposited surface area (LDSA), by directly utilizing the color values of three RGB color models (red, green, and blue) in street view images. Our objective is to combine the street images or videos with pollutant concentrations gathered through mobile monitoring in various environments (urban, suburban, villages, and a harbor city). This approach will allow us to develop neighborhood-level estimation models for pollutant concentrations using deep learning methods, facilitating swift and cost-effective assessment of PM metrics.

2. DATA AND METHODOLOGY

2.1. Measurement Sites. The investigation encompassed four environments and different periods: the urban vicinity of Augsburg (Germany, 09/2018-06/2020), a suburban municipality on the outskirts of Munich (Neubiberg, 04-12/2022), two neighboring villages located on the German-Czech border (Bayerisch Eisenstein (DE) and Zelezna Ruda (CZ), 11/2018), and the residential area at the entrance of the Rostock harbor (Warnemünde, 13-16/09/2022) in Germany (Figure 1).

Figure 1. Locations of the monitoring campaign map

Sampling campaigns were conducted in all four study areas during sunny/cloudy days. In this study, the two walks from summer sampling (walks on 14/08/2018 and 22/08/2018) in Augsburg (Figure S1a) were selected as the basis for model construction, while another two walks from winter sampling (walks on 12/02/2020 and 21/02/2020) served for temporal validation of the model. Furthermore, walks' sampling data from Neubiberg (walk on 11/04/2022) (Figure S1b), Warnemünde (walk on 23/11/2018) (Figure S1c), Bayerisch Eisenstein (walk on 23/11/2018) (Figure S1d), and Zelezna Ruda (walk on 23/11/2018) (Figure S1e) were employed for spatial generalization of the model. In Augsburg (48.37N, 10.90E), the study was conducted within the city center, covering a fixed walking path of approximately 15 km in length,

https://doi.org/10.1021/acs.est.3c06511
Environ. Sci. Technol. 2024, 58, 3869−3882

passing through various types of land use to ensure the representation of different microenvironments (e.g., park, central business district, and traffic) (Figure S1a).[7,30] The average walking time of one route was about 4 h. Neubiberg (48.06N, 11.66E), located about 12 km south of the city center on the outskirts of Munich, was covered by a 5 km long monitoring route passing through densely populated areas such as transport stops, residential areas, parks, metro stations, shops, and restaurants (Figure S1b). Warnemünde (54.18N, 12.08E), harbor area of Rostock, was covered by a mobile measurement route (5 km) passing through the town's densely populated areas such as churches, train stations, stores, and restaurants (Figure S1c). In Bayerisch Eisenstein (49.12N, 13.20E) and Zelezna Ruda (49.14N, 13.24E), the mobile measurements were carried out with fixed routes of approximately 5 and 4 km in length passing through residential areas with little traffic (Figure S1d,e).[3] The walking times for the routes in Neubiberg, Bayerisch Eisenstein, Zelezna Ruda, and Warnemünde were approximately 1−1.5 h.

2.2. Collection of the Measurement Data, Instrument Preparation, and Processing Protocols. The latest version of the mobile platform used in Warnemünde and Neubiberg is described in detail in another study from Bendl et al.[31] and the similar previous version of the stroller with the comparable properties in the study from Bayerisch Eisenstein and Zelezna Ruda, where similar devices were used.[3] Mobile measurements of ambient PM, including PM_X ($PM_{1.0}$, $PM_{2.5}$, PM_{10}), UVPM, BC, BrC, PNC, and LDSA, were conducted using a mobile trolley (Figure S2). Particle size distributions were measured using an optical particle sizer (OPS) (3330, TSI, USA) with a time resolution of 1 s, and subsequently, $PM_{1.0}$, $PM_{2.5}$, and PM_{10} were converted from the number to mass concentrations. PNC, within the size range of 20−1000 nm, was measured by condensation particle counters (P-Trak 8525, TSI, USA/testo DiSCmini, testo, DE). LDSA was monitored by the testo DiSCmini—hand-held measuring device for the number of nanoparticles (Testo, Germany). The equivalent mass concentrations of BC (eBC) and eUVPM were determined from the light absorption at 375 and 880 nm, respectively, using a microaethalometer (MA200, AethLabs, USA) with a time resolution of 10 s. Equivalent BrC (eBrC) was calculated by subtracting eBC (880 nm) from eUVPM (375 nm). In addition, a GPS (64s, Garmin, USA; recording resolution 1 s) was installed to register the location, and the point-of-view camera (Tough TG Tracker, Olympus, Janpen) was set as follows: the time was set 5 s; the brightness (exposure compensation) was set as 0.0; the lighting conditions was set as auto; the field of view was set as wide; and the image size was set as 4K (3840 × 2160 pixels). The instruments were placed in waterproof aluminum boxes mounted on the trolleys, and omnidirectional sample inlets were positioned at a height of approximately 1.5 m, corresponding to the breathing zone of adults. Additional detailed information about the instrumentation has been provided in the literature.[30,31]

Prior to each measurement campaign, instrument preparation was conducted in the laboratory, including zero calibration checks, replacement of the MA200 filter strip, battery and memory checks, and time synchronization of all instruments. Flow measurements were performed by using a factory calibrated flow meter (4043 H, TSI, USA). All instruments in this study have specific timers inside (day/month/year). The timers of all instruments were synchronized at the beginning of the experiment. Since the instruments recorded data with different temporal resolutions, the synchronized measured aerosol concentrations were smoothed using the central moving average method.[32]

As mentioned in our previous study, the angle of the camera may affect the model prediction results (only a 204° angle was used in the presented study). For example, small differences in the vertical tilt angle of the camera can greatly change the street view image. Therefore, during the sampling process, we have been carefully ensured that the camera and the trolley are parallel and not blocked to keep all the variables were constant during our experiments (Figure S2). In addition, to ensure the standardization of image acquisition, we excluded images obtained during the equipment debugging phase as well as those captured when the camera temporarily stopped due to lower battery power. This filtering process ensures that the selected images in our data set represent the target category, possessing clarity and high resolution.

2.3. Integration of the Data Matrix. In order to address the disparity in frequencies between the street view images (5 s) and the pollutant monitoring data (i.e., PM_X, PNC, and LDSA in 1 s; eUVPM, eBC, and eBrC in 10 s), a data integration strategy was implemented. The integration process involved selecting data points from the pollutant monitoring times that coincided with the specific moments when the photographs were captured.

To achieve this, the least common multiple of the frequency values was determined. By aligning the data at this common multiple time step, we ensured that the street view images and pollutant monitoring data were synchronized for integration. Specifically, the data points from the pollutant monitoring time series were matched with the corresponding time instances of the captured photographs.

2.4. Street View Imagery Color Model. In one time sequence of sampled street images (4h), one street image was captured every 5 s; approximately 2800 images were captured. Each image has a resolution of 3840 × 2160, meaning a length of 3840 pixels and a width of 2160 pixels. In the red (R), green (G), and blue (B) color space, the color of each pixel can be represented by a combination of RGB components. Each component can range from 0 to 255, providing a ternary value (R, G, and B) for each pixel. Therefore, the total number of information is calculated as 3 × 3840 × 2160.

First, we extracted the color luminance values for red, green, and blue via Python software Open Source Computer Vision Library (OpenCV library). Then construct a color histogram of the image, i.e. calculate the proportion of different colors in the image. With bins = 256, each point on the horizontal axis corresponds to a specific color value, while the vertical axis indicates the number of pixels in the image that possess that particular color value.

Then RGB converts to HSV (hue, saturation, value), due to HSV proves to be better suited for depicting human color perception and offers greater benefits in the realm of image processing.[33] The expression for the transformation from RGB to HSV is as follows

https://doi.org/10.1021/acs.est.3c06511
Environ. Sci. Technol. 2024, 58, 3869−3882

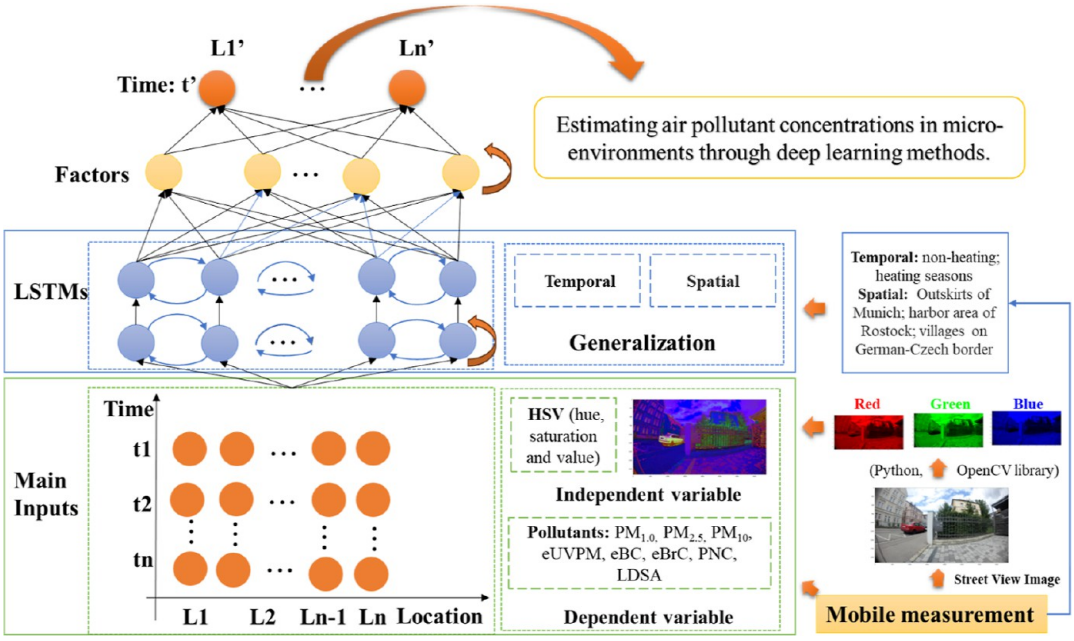

Figure 2. Network framework of the LSTME model for the air pollutant concentration prediction. The main inputs [dependent variable: monitoring PM metrics concentration data, independent variable: HSV, (hue, saturation, value)] are included in orange solid boxes; A recursive arrow indicates that the processing of this layer can be repeated.

$$H = \begin{cases} \dfrac{60(G - B)}{V - \min(R, G, B)} & \text{if } V = R \\ 120 + \dfrac{60(G - B)}{V - \min(R, G, B)} & \text{if } V = G \\ 240 + \dfrac{60(G - B)}{V - \min(R, G, B)} & \text{if } V = B \end{cases} \quad (1)$$

$$S = \begin{cases} \dfrac{V - \min(R, G, B)}{V} & \text{if } V \neq 0 \\ 0 & \text{otherwise} \end{cases} \quad (2)$$

$$V = \max(R, G, B) \quad (3)$$

Additionally, we recorded the high-frequency instances of HSV values in image histograms and included them as independent variables in the model. Given that S and V remain consistent throughout the sampling process, our emphasis will primarily be on the frequency distribution of H values as they exhibit significant variability.

2.5. Model Development and Prediction Variables. In this study, we established the LSTM model to estimate PM metrics concentration. LSTM is a type of RNN that is capable of learning from long-term dependent information.[34] It has been successfully applied in the field of air pollution.[35] The overall estimation framework is shown in Figure 2.

At the beginning of setting the models, the training and testing data splitting proportions were set as 50:50, 60:40, 70:30, 80:20, and 90:10 for each model to select the best splitting proportion for deep learning. Meanwhile, to investigate the advantages of LSTM, this study also compares the LSTM model with other deep learning models [RNN (recurrent neural network) and GRU (gated recurrent unit)]. RNN is an algorithm for deep learning in the field of artificial intelligence.[36] It captures sequence information through network nodes and can achieve particularly good results based on processing time series events. GRUs were introduced as a variation of RNNs to address the vanishing gradient problem. It employs gating mechanisms that control the flow of information within the network, allowing us to selectively retain or update information over time. GRUs have fewer parameters compared with traditional RNNs and can be more computationally efficient.

2.6. Model Accuracy Evaluation Method. The evaluation of the model's accuracy can capture both its fitting effect and error. Initially, the training set is utilized to derive the regression equation, followed by testing the resulting model using the validation set to assess its performance. This approach helps strike a balance between the model's deviation and variance. Specifically, 70% of the data from a complete mobile monitoring route are allocated as the training set, while the remaining 30% is set aside as the verification set. Furthermore, to validate the model's accuracy, another complete monitoring route from the same period is also chosen as the validation set.

The present study assesses the temporal generalization of the model by examining its performance on two walking samples collected along the same route during the heating season in Augsburg. Additionally, the model's spatial generalization is evaluated by applying it to three different regions: Suburbs of Munich (Neubiberg), Villages at the German-Czech border (Bayerisch Eisenstein and Zelezna Ruda), and German harbor city (Warnemünde). This allows for an evaluation of the model's generalization across different geographical areas. The accuracy of the model is reflected by examining the closeness between the simulated results of the verification set and the actual observation values. This study employs several evaluation indicators: the correlation coefficient (R^2), root mean squared error (RMSE), mean absolute error (MAE), fitting index (index of agreement, IA), and slope of the regression (slope). The correlation coefficient (R^2) represents the model's fitting effect, while RMSE and MAE

https://doi.org/10.1021/acs.est.3c06511
Environ. Sci. Technol. 2024, 58, 3869−3882

Table 1. Average Concentrations of PM Metrics in Downtown Augsburg (AUG), Neubiberg (NEU), Warnemünde (WAR), Villages [Bayerisch Eisenstein (BE), and Zelezna Ruda (ZR)] (Unit: $PM_{1.0}$, $PM_{2.5}$, PM_{10}, eUVPM, eBC, and eBrC, $\mu g/m^3$; PNC, #/cm^3, and LDSA, $\mu m^2/cm^3$)[a]

site	monitoring time	$PM_{1.0}$	$PM_{2.5}$	PM_{10}	eUVPM	eBC	eBrC	PNC	LDSA
AUG	nonheating season	1.0 ± 2.3	2.1 ± 4.6	6.4 ± 11.7	0.74 ± 1.00	0.87 ± 0.85	0.31 ± 0.85	5028 ± 23,670	12.2 ± 14.9
AUG	heating season	1.2 ± 0.9	2.7 ± 1.4	9.9 ± 9.1	1.47 ± 0.66	1.02 ± 0.65	0.4 ± 0.21	8355 ± 71,266	19.0 ± 33.5
NEU	heating season	0.4 ± 0.1	1.3 ± 1.0	9.3 ± 25.9	0.45 ± 0.43	0.54 ± 0.48	0.18 ± 0.13	5857 ± 25,085	11.7 ± 11.5
WAR	nonheating season	1.1 ± 3.9	5.2 ± 10.0	14.3 ± 18.7	0.20 ± 0.23	0.20 ± 0.20	0.01 ± 0.30	17,746 ± 20,660	13.0 ± 32.0
BE	heating season	9.6 ± 2.4	10.6 ± 2.4	10.9 ± 2.7	2.21 ± 1.73	1.80 ± 1.93	1.73 ± 1.06	4678 ± 8476	
ZR	heating season	9.5 ± 5.8	11.6 ± 5.9	12.0 ± 7.0	3.40 ± 2.50	1.70 ± 1.48	1.65 ± 1.61	7067 ± 12,321	

[a]Non-heating seasons: (May−October) heating seasons (Nov.−Apr.).

gauge the deviation between predicted and true values. IA measures the consistency between the predicted and true values. By combination of these four indicators, a more comprehensive evaluation of the obtained model can be conducted. Data processing and statistical analyses were performed using Pycharm software (professional version 2022.2.2), Python (v3.8.15), and PyTorch (v2.0, cuda 11.8).

3. RESULTS AND DISCUSSION

3.1. Aerosol Concentrations in Different Locations. The mobile monitoring aerosol data used in this study are supplied by our previous studies in the urban of Augsburg,[7,30] German-Czech border villages,[3] and campaigns in Neubiberg (performed during 04-12/2022) and Warnemünde (performed during 13-16/09/2022). The average concentrations of PM metrics from the selected walks in downtown Augsburg, Neubiberg, Warnemünde and villages (Bayerisch Eisenstein and Zelezna Ruda) are shown in Table 1. It was discovered that the concentrations of $PM_{2.5}$ and PM_{10} in all areas were meeting the 24 h average of the World Health Organization (WHO) air quality guidelines (AQG) of 15 and 45 $\mu g/m^3$, respectively.[37] Furthermore, a detailed analysis of spatiotemporal variability of aerosol in urban and village has been provided in our previous studies.[3,7,30]

3.2. Correlations Among Aerosol Parameters. Pearson correlation analyses were conducted for monitoring walks to investigate the relationships among the aerosol concentration variables within the study area. There were often significant linear correlations between atmospheric PM metrics, but changes in sources and atmospheric processes caused by external factors inevitably alter the correlations between the PM metrics accordingly.[38] As shown in Figure 3, for the selected urban walks, the scatter distributions among $PM_{1.0}$, $PM_{2.5}$, and PM_{10}, among eUVPM, eBC, and eBrC, and between PNC and LDSA tend to form straight lines. This indicated a significant linear positive correlation among them. While the relationships between other PM metrics pairs, such as $PM_{1.0}$ vs eBC, demonstrated a certain level of nonlinear correlation. This was further investigated by Spearman analysis of their correlations (Figure S3). Furthermore, there was some volatility in the correlations among the concentrations of the individual PM metrics. In particular, when comparing the two walks in the nonheating season (May−Oct) and the two walks in the heating season (Nov.−Apr.) (Figures 3a,b and S3), there were significant differences in the correlations between the pollutant concentrations. There was significant variation in the correlation between pollutant concentrations. This indicated that the correlation between pollutants PM metrics was noticeably influenced by seasonal changes and was also related to multiple factors such as pollution emissions and meteorological conditions.[39,40] Moreover, we performed an analysis of the correlation among different PM metrics in additional regions (Figure S4). The findings further indicated the existence of specific linear associations between pairs of PM metrics, including $PM_{1.0}$, $PM_{2.5}$, and PM_{10} pairs; eUVPM, eBC, and eBrC pairs; as well as PNC and LDSA pairs. These results suggested spatial homogeneity in the correlations between these PM metric pairs.

3.3. Modeling and Interpretation of Air PM Metrics on Urban Areas. Leveraging LSTM models, we created estimation models for $PM_{1.0}$, $PM_{2.5}$, PM_{10}, eUVPM, eBC, eBrC, PNC, and LDSA in urban settings. The models used monitoring of street images together with the corresponding PM metric concentrations. In this study, mobile monitoring data of two walks from summer monitoring were selected to establish the model. Based on the optimized fitting effects for all PM metrics, 70:30 was chosen as the best splitting proportion (Figure S5); hence, 70% of one walk monitoring data were used as the training set to train the model and debug the model according to its error until convergence (Figure 4-left). In order to validate the model, in addition to 30% of the same sampling as the model validation set mentioned above, a new regular walk monitoring data set in summer was additionally added in the validation set (Figure 4-right). Based on the evaluation indicators (R, RMSE, MAE, IA, and Slope), the LSTM model had a better performance in both the test and validation sets, as shown in Figure 3, with 85, 92, 79, 97, 98, 98, 86, and 96% of the variations explained for $PM_{1.0}$, $PM_{2.5}$, PM_{10}, eUVPM, eBC, eBrC, PNC, and LDSA in validation sets, respectively. Additionally, we conducted a separate analysis on the accuracy of the 30% subsample using both the same sampling and the new regular walk approaches to demonstrate the differences between the two holdout methods (Table S1). The results indicate that the explanatory power for the variation in the eight PM metrics is consistently high in both validation data sets, and the differences between them are minimal.

Through an examination of the distribution data of HSV values in the input variable images, it has been found that the hue values, which serve as the primary variable, tend to concentrate around 0, 30, 75, 110, 120, and 165. These specific values predominantly represent objects such as buildings, cars, grass, roads, trees, and the sky in the images, aligning with our previous findings.[7,41] It is important to note that in contrast to our previous studies, the model introduced in this research does not delve into the structural aspects of images. Instead, it directly extracts color information, resulting in improved outcomes. We conducted an in-depth error analysis of key parameters, including neighboring HSV values, to assess the uncertainty associated with different hues. The results showed

https://doi.org/10.1021/acs.est.3c06511
Environ. Sci. Technol. 2024, 58, 3869−3882

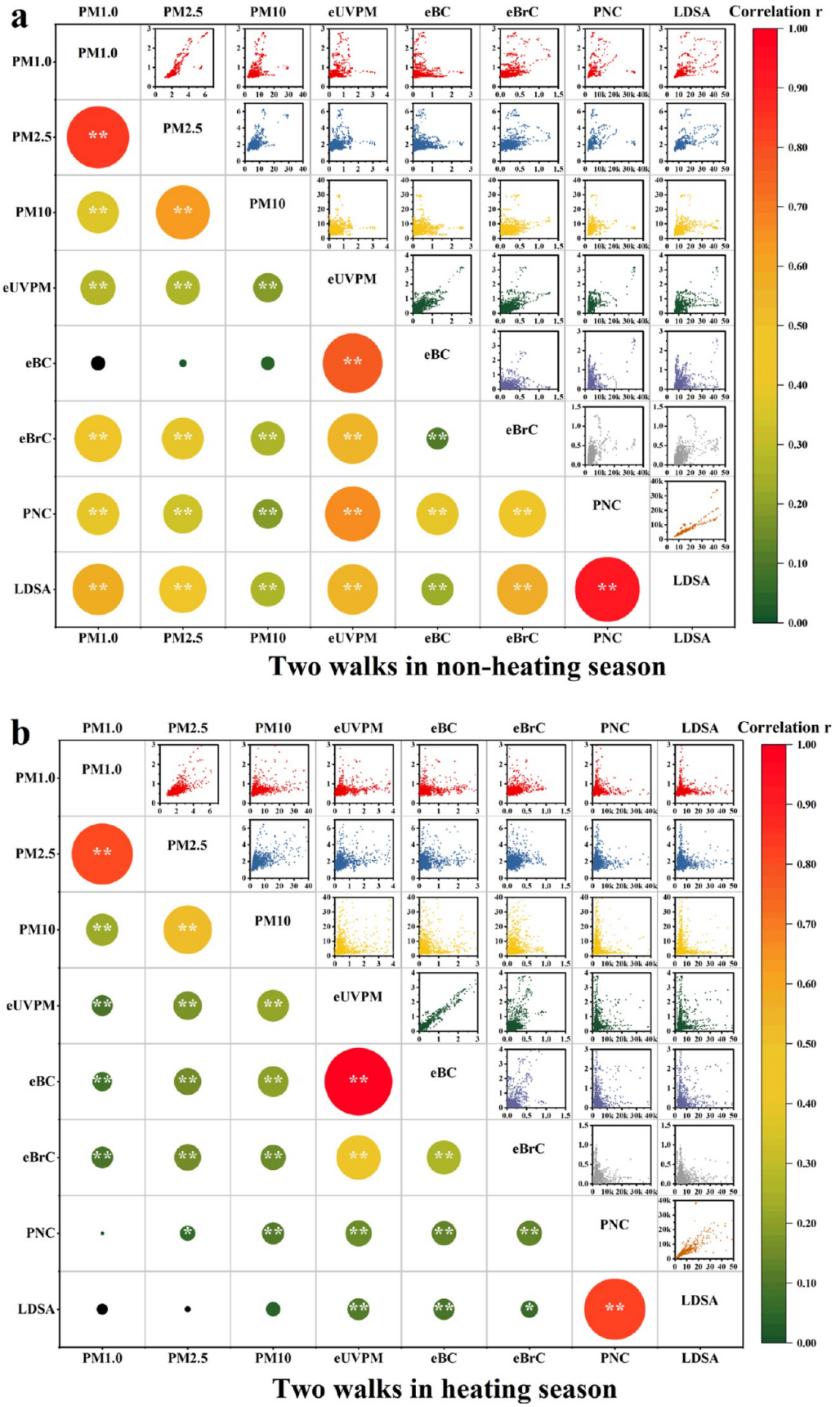

Figure 3. Pearson correlation analysis among parameters during different seasons ((a) two walks in the nonheating season; (b) two walks in the heating season) in the downtown of Augsburg (*, $p < 0.05$; **, $p < 0.01$)

https://doi.org/10.1021/acs.est.3c06511
Environ. Sci. Technol. 2024, 58, 3869−3882

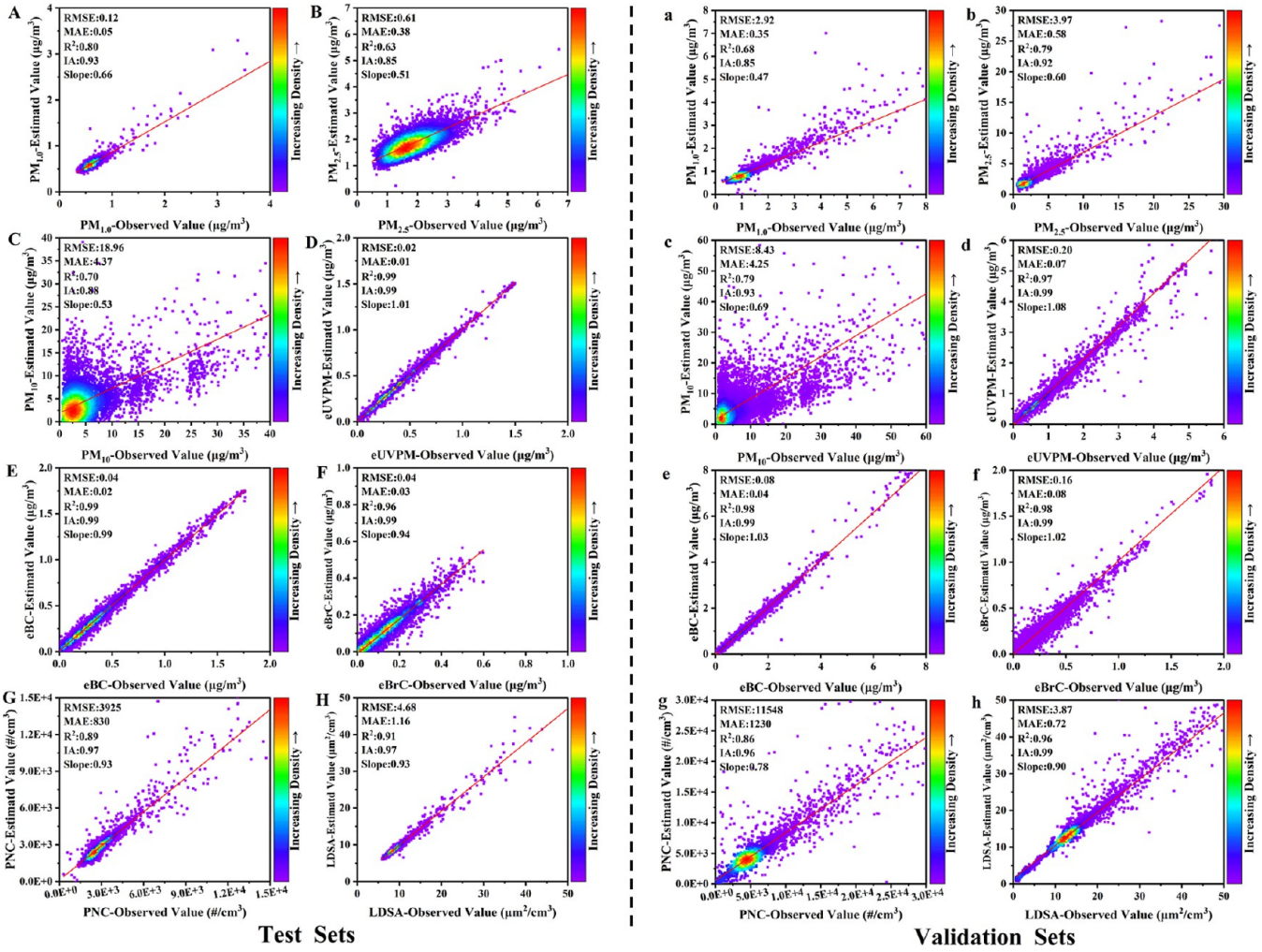

Figure 4. Observed value with the estimation for $PM_{1.0}$, $PM_{2.5}$, PM_{10}, eUVPM, eBC, eBrC, PNC, and LDSA from the Long Short-Term Memory (LSTM) model; left panel, test sets (70% data of one walk); right panel, validation sets (the remaining 30% data of the walk and one entire walk) in the downtown of Augsburg.

that even with alterations in hue, the variations in model evaluation metrics were minimal, and satisfactory prediction results were consistently achieved (Figure S6). This suggests that the changes in the HSV values and key parameters have minor effects. Additionally, data normalization is allowed for similar results, despite concurrent hue changes. This reinforces the model's credibility in assessing air pollution concentrations. This further validated our proposed model in evaluating air pollution concentrations.

3.4. Comparison of Deep Learning Methods. To investigate the performance of the LSTM model, we developed separate concentration estimation models for each pollutant using two additional deep learning models (RNN and GRU) for the same data set as discussed above. These models were tested and validated using the same test and validation sets as those applied for the LSTM model. Athira et al. (2018) conducted a study comparing the performance of RNN, LSTM, and GRU models.[42] They found that the GRU achieved the highest prediction accuracy among the three models. Building upon this, Wang et al. (2018) introduced residual connectivity to both LSTM and GRU models and compared their prediction results.[43] The experimental findings indicated that GRU still exhibited a higher accuracy even with the inclusion of residual connectivity.

In this study, logarithmic conversion of concentration was not employed to enable a comparison between models. The result showed that these three models have the capability of simultaneously estimating the air pollutant concentrations of all walking location, indicating their capability to represent high-level spatiotemporal features.[35]

We compared the performance of the three models in terms of convergence speed, including the loss function (LOSS) and RSME. First, we standardized the data for these indicators and then separately trained them on the training sets until the values of the LOSS and RSME stabilized. With the increase of training iterations, the values of the LOSS and RSME showed an overall decreasing trend (Figure S7). This indicates that the error between the predicted values and actual values gradually decreased, and the model achieved a better predictive effect on the training set. When comparing the three models, we found that the LSTM model demonstrated a faster convergence speed in all of the metrics.

Subsequently, we integrated the estimation performance after each estimation (Table S2). Despite the strong performance of the RNN and GRU models on the test and validation sets, particularly for eUVPM, eBC, and eBrC, which even outperformed our previous results with random forest models,[7,41] their performance was on par with that of LSTM.

https://doi.org/10.1021/acs.est.3c06511
Environ. Sci. Technol. 2024, 58, 3869−3882

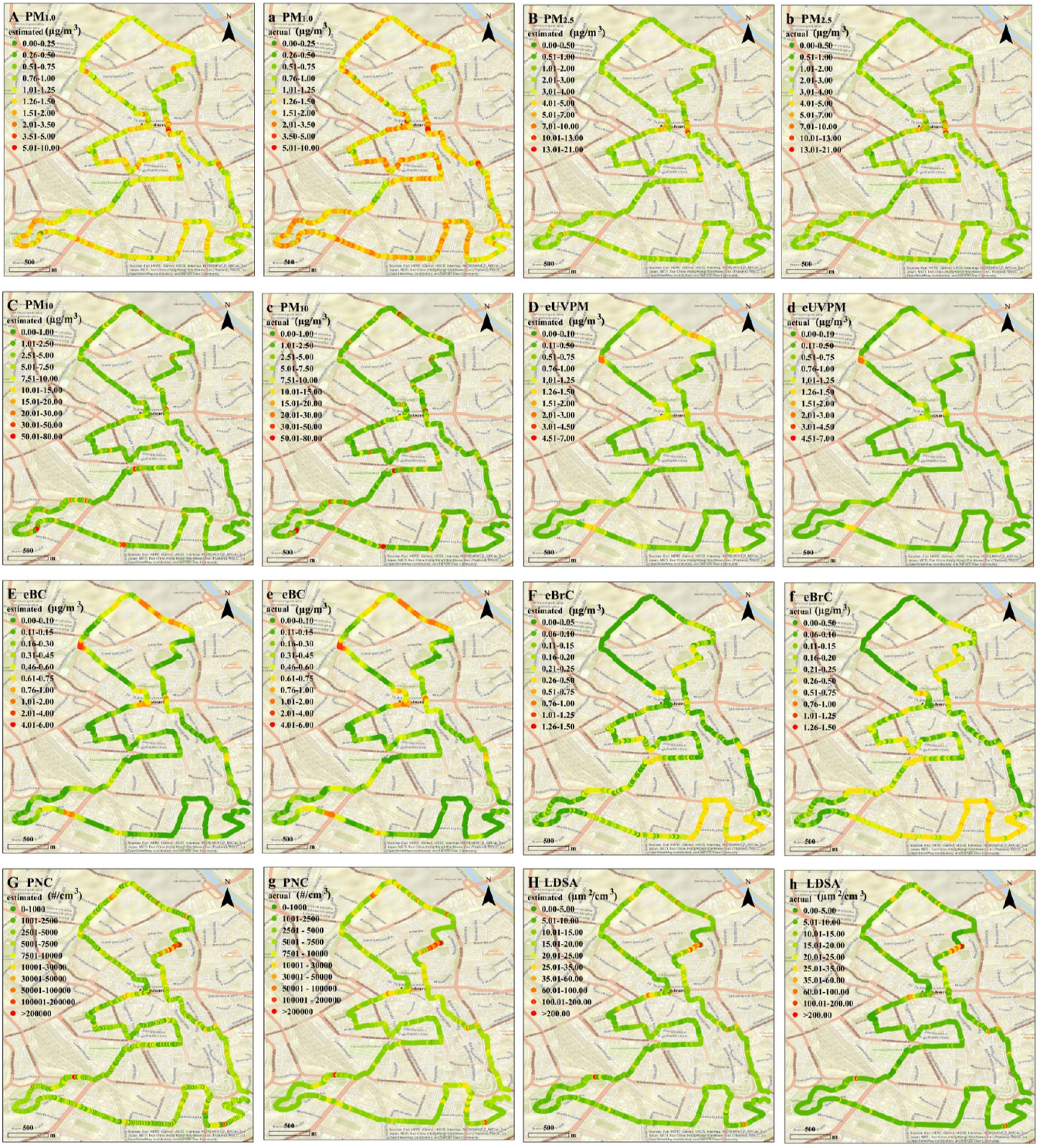

Figure 5. Spatial distribution estimates of eight air PM metrics using the LSTM-HSV model (A−H, capital letters) compared with actual monitoring (a−h, lowercase) in the downtown of Augsburg

However, when it comes to PNC, $PM_{1.0}$, $PM_{2.5}$, and PM_{10}, LSTM is capable to predict each of these PM metrics. The primary factors contributing to this phenomenon can be attributed to two aspects. First, it was likely influenced by the variations in resolution of the measurement data and how each model handles the image-related data specific to their respective approaches. Second, it was also associated with the frequent and rapid fluctuations observed in PM_X and PNC data within short time intervals. These fluctuations posed a challenge, particularly for GRU and RNN models, suggesting a comparatively simpler architecture compared to LSTM. Consequently, the handling of such data dynamics by GRU and RNN models was moderately less efficient. In contrast, the LSTM model addressed this limitation by introducing a sophisticated gating mechanism that amalgamates short-term memory with long-term memory. This novel gating system enhanced information discernment and enabled effective simulation of multiple inputs. As supported by research

https://doi.org/10.1021/acs.est.3c06511
Environ. Sci. Technol. 2024, 58, 3869−3882

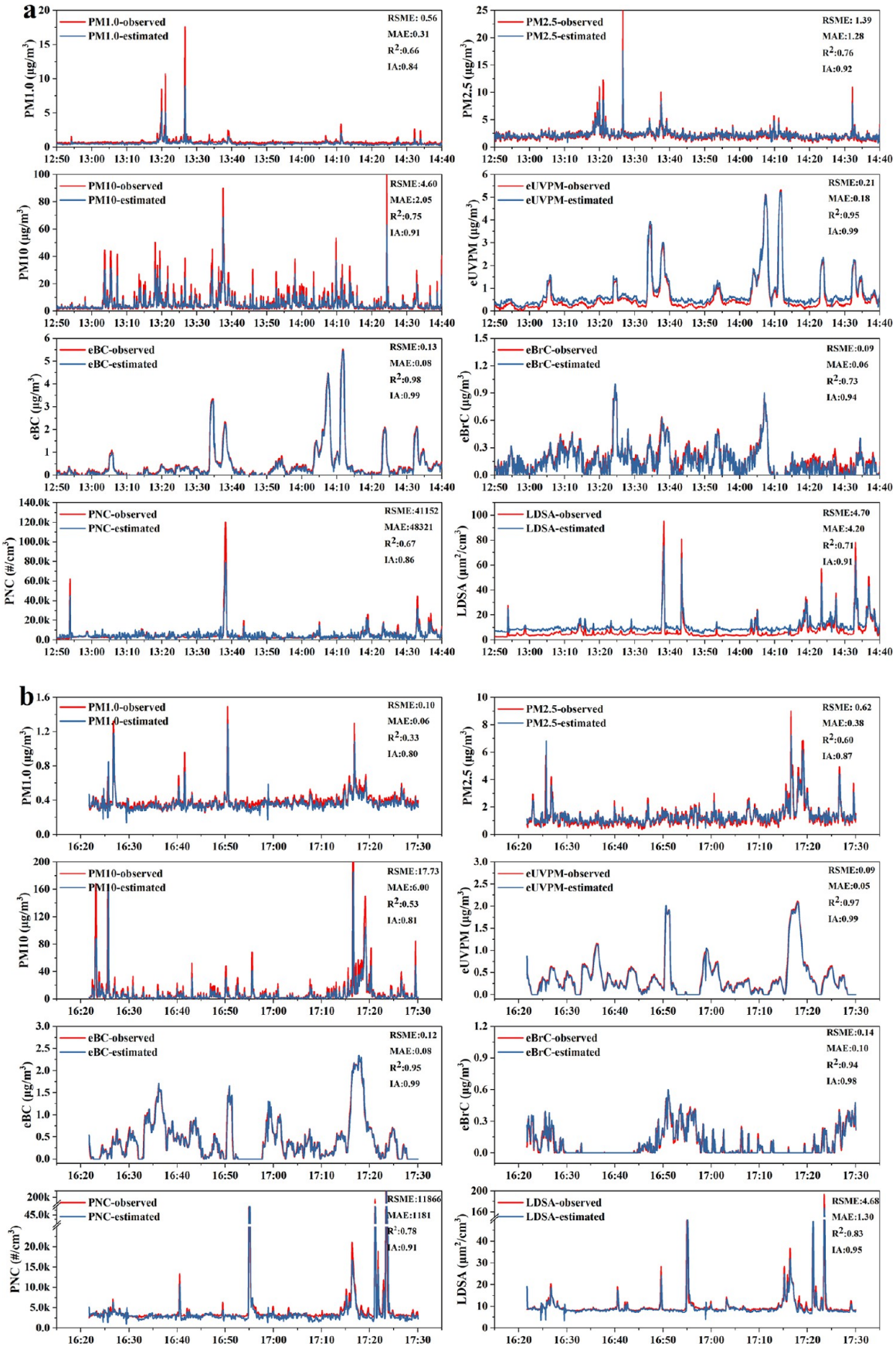

Figure 6. continued

https://doi.org/10.1021/acs.est.3c06511
Environ. Sci. Technol. 2024, 58, 3869−3882

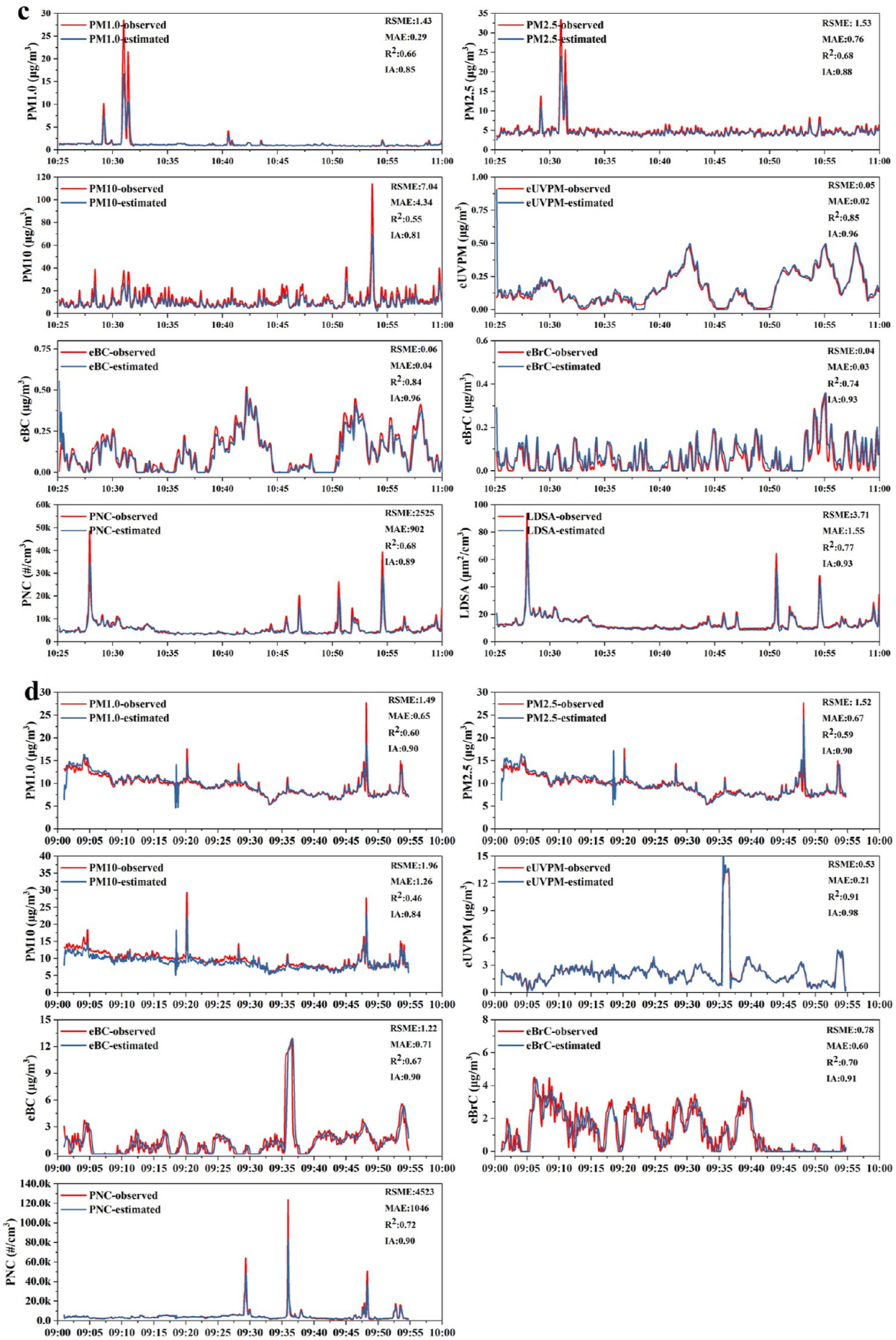

Figure 6. continued

https://doi.org/10.1021/acs.est.3c06511
Environ. Sci. Technol. 2024, 58, 3869−3882

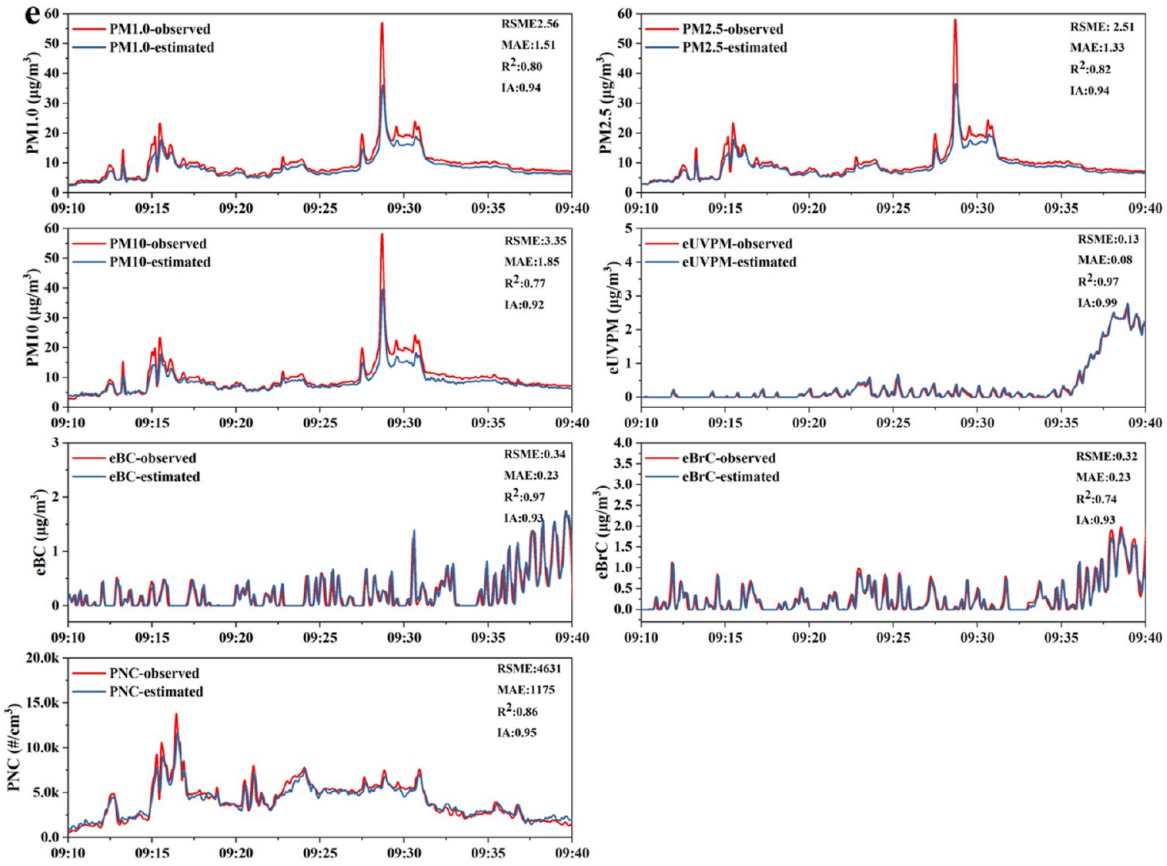

Figure 6. Generalization of the developed LSTM-HSV model for the estimation of individual air PM metrics in temporal ((a) one walk in the heating season in the downtown of Augsburg) and spatial (b) one walk in the outskirts of Munich, Neubiberg; (c) one walk in the harbor zone of Rostock, Warnemünde; and (d,e) two walks in neighboring villages at the German-Czech border, Bayerisch Eisenstein, and Zelezna Ruda).

studies,[15,16] the LSTM model exhibited better performance in processing time-series problems. Furthermore, these findings indicated that the LSTM model is better equipped to capture the complex spatiotemporal variability associated with various PM metrics.[35]

Simultaneously, the model's estimated concentrations were visualized to demonstrate their practical applicability. In Figure 5, the LSTM-HSV model effectively identifies the hotspots at their respective locations and distinguishes between varying microenvironmental concentrations, as demonstrated by the comparison between estimated and actual measured concentrations for the eight PM metrics in the validation sets. Overall, the estimated concentrations of all PM metrics in different microenvironments exhibited trends similar to those of the actual measured concentrations, thus further validating the practicality of the LSTM-HSV model. In summary, the LSTM-HSV model serves as a valuable tool for estimating spatiotemporal variations of aerosols, complementing fixed-site measurements of aerosol pollutants in health risk assessment and long-term public health improvement efforts.

3.5. LSTM-HSV Model Generalization. To evaluate the overall applicability of the LSTM-HSV model, we conducted a thorough assessment, considering both temporal and spatial aspects. To investigate the transferability of the model to other seasons, we used the same walking path in Augsburg but with data measured during the heating season. To investigate the spatial dimension, we extended the analysis to include three sampling surveys in different locations: the outskirts of Munich (Neubiberg), the harbor of Rostock (Warnemünde), and two villages situated on the Germany-Czech border [Bayerisch Eisenstein (D) and Zelezna Ruda (CZ)]. These sampling walks were carried out in various times of the year, namely, April, September, and November. This approach allowed us to examine the model's performance across differently characterized locations and seasons, further enhancing its robustness and applicability. Initially, we individually applied LSTM, RNN, and GRU to analyze the data from each site. The outcomes indicated that all the three models exhibited better predictive capabilities for the eight PM metrics (Table S3). However, in an overall assessment, LSTM demonstrated better predictive capabilities in both temporal and spatial dimensions, further underscoring its effectiveness.

Figure 6a demonstrates the utilization of the LSTM-HSV model, originally set up for summer sampling, to forecast pollutant concentrations during winter. The predictions were then compared to the actual monitored pollutant concentrations (Figures 6a and S8). The results revealed a consistent pattern of variability between the predicted and the observed concentrations for each pollutant. Notably, the R^2 values for eUVPM and eBC exceeded 0.8, while the R^2 values for the remaining PM metrics were also above 0.65. These findings suggest the LSTM-HSV model's capability to generalize across different seasons.

Additionally, the model's ability to estimate PM metric concentrations in various locations is demonstrated in Figures 6b–e, and S9–S11. Figure 6b showcases its performance for one walk in the outskirts of Munich (Neubiberg), while Figure 6c highlights its performance during a walk in the harbor of

https://doi.org/10.1021/acs.est.3c06511
Environ. Sci. Technol. 2024, 58, 3869−3882

Rostock (Warnemünde), both in the nonheating season. Furthermore, Figure 6d,e displays its effectiveness in estimating PM metrics levels during the heating season for two walks in neighboring villages [Bayerisch Eisenstein (DE) and Zelezna Ruda (CZ)]. The results further confirm that the LSTM-HSV model exhibits spatial generalizability, particularly for eUVPM, eBC, eBrC, and LDSA, with an impressive R^2 value exceeding 0.8. However, for PM_X, the R^2 values were relatively lower, primarily due to the utilization of different monitoring instruments in suburban and rural sampling campaigns. Meanwhile, the model was also able to capture the peaks of each PM metrics. This is mainly because the LSTM model captured and recorded the features of the test set when the peaks appeared in the construction of the prediction model, thus effectively predicting the peaks. Compared with different PM metrics at the same site, the developed model has an accurate estimation of the peaks of eUVPM and eBC in particular, mainly because the time frequency of these two metrics was 10s, which made them vary less drastically.

Scatter plots between the measured and estimated values of the eight PM metrics in different regions show that the proposed concentration estimation model can be applied to different concentrations with slopes close to 1 (Figures S10 and S11). This means that the model can also achieve the expected estimation results when applied in different regions. This spatial generalization ability allows the LSTM-HSV model to better estimate various PM indicators in different geographical areas and regions. Concurrently, the model's projected concentrations were depicted in a visual form to showcase their real-world usefulness in suburban, harbor, and two village settings (Figures S12−S14). The findings likewise affirm that these estimations aptly capture the spatial fluctuations of diverse indicators and proficiently pinpoint their specific focal points within each area. This underscores the pragmatic value of the model's projections.

3.6. Uncertainty of the LSTM-HSV Model. The main sources of bias in the LSTM model for modeling aerosol pollutant concentrations are as follows: (i) the quality and representativeness of the street image data can directly and significantly influence the accuracy of the model's fit. For instance, the uncertainty of the camera (e.g., camera position, camera angle, camera resolution, and overall brightness of the image) during the sampling process can adversely affect the quality of the photos, potentially leading to decreased accuracy in estimating aerosol concentrations. Similarly, the use of different camera models during sampling may result in varying the pixel quality, introducing corresponding differences in the estimation process. Hence, to ensure the reliability of the data, it is crucial to continuously monitor the camera's status throughout the entire sampling process to keep all the variables constant during the experiments. (ii) Concerning the input independent variables, the absence of meteorological indicators during the sampling process, which were not collected alongside the mobile monitoring equipment, could introduce certain inaccuracies to the model. For instance, the dispersion conditions can affect the PM metrics concentrations.[7] Li et al. (2017) employed LSTM to enhance $PM_{2.5}$ prediction by incorporating meteorological indicators as auxiliary variables within the model,[35] yielding improved outcomes. Thus, it is advisable to concurrently monitor meteorological indicators during future mobile monitoring processes to include them in the model. (iii) The uncertainty in LSTM models for predicting ambient PM concentrations arises from their reliance on a significant amount of training data to achieve effective learning, and the present study did not include narrow street canyons with high traffic. Consequently, accurate predictions in specific microenvironments often require extended sampling durations to accumulate a sufficiently large data set, enabling the LSTM model to capture underlying patterns and improve prediction accuracy. (iv) In this study, LSTM is utilized to characterize the relationship between HSV attributes and atmospheric pollutant concentrations using street images, aiming at predicting pollutant levels. However, a short prior sampling of the study area is necessary to collect specific data before constructing the model due to the variability of air pollution in different countries and even in different cities. When the data adhere to the same distribution, there is an enhancement in the generalizability effect. Conversely, when the data do not share an identical distribution, it becomes essential to gather a larger data set for model construction. Consequently, the model's performance may be compromised when dealing with long time series data. For instance, the suburban area of Munich exhibited inadequate generalization in this study, suggesting the potential needed to incorporate additional neural networks alongside LSTM to further mitigate this limitation.

4. ENVIRONMENTAL IMPLICATION

This study introduces the LSTM-HSV model as a method to estimate concentrations of eight PM metrics ($PM_{1.0}$, $PM_{2.5}$, PM_{10}, eUVPM, eBC, eBrC, PNC, and LDSA) using street view images data. The LSTM-HSV model is particularly effective in modeling time series with long time dependencies. The model's performance was evaluated using air pollutant concentrations collected from four regions: urban, suburban, villages areas, and the harbor city, obtained through a mobile monitoring platform. Using the same data set from Augsburg summer, a comparative analysis of three different models, namely LSTM, RNN, and GRU, revealed that the LSTM model exhibited better performance over the other algorithms, which was substantiated by improved values in evaluation metrics such as RMSE, MAE, R^2, and IA. Furthermore, the LSTM-HSV model exhibited capability for spatiotemporal generalization, providing a new insight for estimating pollutant concentrations across different locations and time periods.

■ ASSOCIATED CONTENT

Supporting Information

The Supporting Information is available free of charge at https://pubs.acs.org/doi/10.1021/acs.est.3c06511.

Monitoring roads and instruments; correlation analysis among aerosol PM metrics in sampling areas; indicators for evaluating models at different training/validation splits; evaluation metrics for different hue groups; loss function and root mean squared error comparison of various deep learning prediction methods in terms; observed value with the estimation for PM metrics from the LSTM model in sampling areas; spatial distribution estimates of PM metrics using the LSTM-HSV model compared with actual monitoring in sampling areas; and performances of the different walks and the comparison of the performances of the different methods in different campaigns (PDF)

https://doi.org/10.1021/acs.est.3c06511
Environ. Sci. Technol. 2024, 58, 3869−3882

AUTHOR INFORMATION

Corresponding Authors

Xiansheng Liu − *Beijing Key Laboratory of Big Data Technology for Food Safety, School of Computer Science and Engineering, Beijing Technology and Business University, Beijing 100048, China; Institute of Environmental Assessment and Water Research (IDAEA-CSIC), 08034 Barcelona, Spain;* orcid.org/0000-0002-0228-5551; Email: liugar@cid.csic.es

Xun Zhang − *Beijing Key Laboratory of Big Data Technology for Food Safety, School of Computer Science and Engineering, Beijing Technology and Business University, Beijing 100048, China; State Key Laboratory of Resources and Environmental Information System, Beijing 100101, China;* orcid.org/0000-0002-5502-2974; Email: zhangxun@btbu.edu.cn

Authors

Rui Wang − *Beijing Key Laboratory of Big Data Technology for Food Safety, School of Computer Science and Engineering, Beijing Technology and Business University, Beijing 100048, China*

Ying Liu − *Beijing Key Laboratory of Big Data Technology for Food Safety, School of Computer Science and Engineering, Beijing Technology and Business University, Beijing 100048, China*

Hadiatullah Hadiatullah − *School of Pharmaceutical Science and Technology, Tianjin University, Tianjin 300072, China*

Yanning Xu − *School of Environmental and Municipal Engineering, Qingdao University of Technology, Qingdao 266525, China*

Tao Wang − *Shanghai Key Laboratory of Atmospheric Particle Pollution and Prevention, Department of Environmental Science & Engineering, Fudan University, Shanghai 200433, China;* orcid.org/0000-0001-9137-5243

Jan Bendl − *University of the Bundeswehr Munich, Faculty for Mechanical Engineering, Institute of Chemical and Environmental Engineering, 85577 Neubiberg, Germany;* orcid.org/0000-0003-2322-5483

Thomas Adam − *University of the Bundeswehr Munich, Faculty for Mechanical Engineering, Institute of Chemical and Environmental Engineering, 85577 Neubiberg, Germany; Joint Mass Spectrometry Center, Cooperation Group Comprehensive Molecular Analytics, Helmholtz Zentrum München, German Research Center for Environmental Health, Neuherberg 85764, Germany*

Jürgen Schnelle-Kreis − *Joint Mass Spectrometry Center, Cooperation Group Comprehensive Molecular Analytics, Helmholtz Zentrum München, German Research Center for Environmental Health, Neuherberg 85764, Germany;* orcid.org/0000-0003-4846-2303

Xavier Querol − *Institute of Environmental Assessment and Water Research (IDAEA-CSIC), 08034 Barcelona, Spain*

Complete contact information is available at: https://pubs.acs.org/10.1021/acs.est.3c06511

Notes

The authors declare no competing financial interest.

ACKNOWLEDGMENTS

This study is supported by National Natural Science Foundation of China (42101470, 72242106), a grant from State Key Laboratory of Resources and Environmental Information System, in part by the Chunhui Project Foundation of the Education Department of China (HZKY20220053), supported by Project of Natural Science Foundation of Xinjiang Uygur Autonomous Region(2023-D01A57). This study is also supported by the RI-URBANS project (Research Infrastructures Services Reinforcing Air Quality Monitoring Capacities in European Urban & Industrial Areas, European Union's Horizon 2020 research and innovation program, Green Deal, European Commission, contract 101036245). This research is also funded by dtec.bw—Digitalization and Technology Research Center of the Bundeswehr [projects LUKAS and MORE]. Dtec.bw is funded by the European Union—NextGenerationEU and the Germany Federal Ministry of Transport and Digital Infrastructure (BMVI) as part of SmartAQnet (grant no. 19F2003B).

REFERENCES

(1) Vette, A.; Burke, J.; Norris, G.; Landis, M.; Batterman, S.; Breen, M.; Isakov, V.; Lewis, T.; Gilmour, M. I.; Kamal, A.; et al. The near-road exposures and effects of urban air pollutants study (NEXUS): study design and methods. *Sci. Total Environ.* **2013**, *448* (448), 38−47.

(2) Jayanthi, V.; Krishnamoorthy, R. Key airborne pollutants—Impact on human health in Manali, Chennai. *Curr. Sci.* **2006**, *90*, 405−413.

(3) Liu, X.; Schnelle-Kreis, J.; Zhang, X.; Bendl, J.; Khedr, M.; Jakobi, G.; Schloter-Hai, B.; Hovorka, J.; Zimmermann, R. Integration of air pollution data collected by mobile measurement to derive a preliminary spatiotemporal air pollution profile from two neighboring German-Czech border villages. *Sci. Total Environ.* **2020**, *722*, 137632.

(4) Menares, C.; Perez, P.; Parraguez, S.; Fleming, Z. L. Forecasting PM2. 5 levels in Santiago de Chile using deep learning neural networks. *Urban Clim.* **2021**, *38*, 100906.

(5) Kelly, F. J.; Fussell, J. C. Size, source and chemical composition as determinants of toxicity attributable to ambient particulate matter. *Atmos. Environ.* **2012**, *60*, 504−526.

(6) Wang, X.; Klemeš, J. J.; Dong, X.; Fan, W.; Xu, Z.; Wang, Y.; Varbanov, P. S. Air pollution terrain nexus: A review considering energy generation and consumption. *Renewable Sustainable Energy Rev.* **2019**, *105*, 71−85.

(7) Liu, X.; Zhang, X.; Schnelle-Kreis, J.; Jakobi, G.; Cao, X.; Cyrys, J.; Yang, L.; Schloter-Hai, B.; Abbaszade, G.; Orasche, J.; Khedr, M.; Kowalski, M.; Hank, M.; Zimmermann, R. Spatiotemporal Characteristics and Driving Factors of Black Carbon in Augsburg, Germany: Combination of Mobile Monitoring and Street View Images. *Environ. Sci. Technol.* **2021**, *55* (1), 160−168.

(8) Kalapanidas, E.; Avouris, N. Short-term air quality prediction using a case-based classifier. *Environ. Model. Softw.* **2001**, *16* (3), 263−272.

(9) Athanasiadis, I. N.; Kaburlasos, V. G.; Mitkas, P. A.; Petridis, V. Applying machine learning techniques on air quality data for real-time decision support. In *First International Naiso Symposium on Information Technologies in Environmental Engineering (ITEE'2003)*; ITEE: Gdansk, Poland, 2023; pp 51−57.

(10) de Hoogh, K.; Wang, M.; Adam, M.; Badaloni, C.; Beelen, R.; Birk, M.; Cesaroni, G.; Cirach, M.; Declercq, C.; Dėdelė, A.; et al. Development of land use regression models for particle composition in twenty study areas in Europe. *Environ. Sci. Technol.* **2013**, *47* (11), 5778−5786.

(11) Seika, M.; Harrison, R. M.; Metz, N. Ambient background model (ABM): development of an urban Gaussian dispersion model

and its application to London. *Atmos. Environ.* **1998**, *11* (32), 1881−1891.
(12) Malcolm, A. L.; Manning, A. J. Testing the skill of a Lagrangian dispersion model at estimating primary and secondary particulates. *Atmos. Environ.* **2001**, *35* (9), 1677−1685.
(13) Wolf, K.; Cyrys, J.; Harciníková, T.; Gu, J.; Kusch, T.; Hampel, R.; Schneider, A.; Peters, A. Land use regression modeling of ultrafine particles, ozone, nitrogen oxides and markers of particulate matter pollution in Augsburg, Germany. *Sci. Total Environ.* **2017**, *579*, 1531−1540.
(14) Stockie, J. M. The mathematics of atmospheric dispersion modeling. *SIAM Rev.* **2011**, *53* (2), 349−372.
(15) Bai, S. N.; Shen, X. L. PM2. 5 prediction based on LSTM recurrent neural network. *Comput. App. Softw.* **2019**, *36* (01), 67−70.
(16) Huang, W.; Cao, Y.; Cheng, X.; Guo, Z. Research on air quality prediction based on improved long short-term memory network algorithm. *PeerJ Comput. Sci.* **2022**, *8*, No. e1187.
(17) Hankey, S.; Marshall, J. D. On-bicycle exposure to particulate air pollution: Particle number, black carbon, PM2. 5, and particle size. *Atmos. Environ.* **2015**, *122* (122), 65−73.
(18) Messier, K. P.; Chambliss, S. E.; Gani, S.; Alvarez, R.; Brauer, M.; Choi, J. J.; Hamburg, S. P.; Kerckhoffs, J.; LaFranchi, B.; Lunden, M. M.; Marshall, J. D.; Portier, C. J.; Roy, A.; Szpiro, A. A.; Vermeulen, R. C. H.; Apte, J. S. Mapping Air Pollution with Google Street View Cars: Efficient Approaches with Mobile Monitoring and Land Use Regression. *Environ. Sci. Technol.* **2018**, *52* (21), 12563−12572.
(19) Wu, D.; Gong, J.; Liang, J.; Sun, J.; Zhang, G. Analyzing the influence of urban street greening and street buildings on summertime air pollution based on street view image data. *ISPRS Int. J. Geoinf.* **2020**, *9* (9), 500.
(20) Qi, M.; Hankey, S. Using street view imagery to predict street-level particulate air pollution. *Environ. Sci. Technol.* **2021**, *55* (4), 2695−2704.
(21) Nathvani, R.; Vishwanath, D.; Clark, S. N.; Alli, A. S.; Muller, E.; Coste, H.; Bennett, J. E.; Nimo, J.; Moses, J. B.; Baah, S.; et al. Beyond here and now: Evaluating pollution estimation across space and time from street view images with deep learning. *Sci. Total Environ.* **2023**, *903*, 166168.
(22) Xia, Y.; Yabuki, N.; Fukuda, T. Development of a system for assessing the quality of urban street-level greenery using street view images and deep learning. *Urban For. Urban Green.* **2021**, *59*, 126995.
(23) Zhao, T.; Liang, X.; Tu, W.; Huang, Z.; Biljecki, F. Sensing urban soundscapes from street view imagery. *Comput. Environ. Urban Syst.* **2023**, *99*, 101915.
(24) Feng, L.; Yang, T.; Wang, Z. Performance evaluation of photographic measurement in the machine-learning prediction of ground PM2. 5 concentration. *Atmos. Environ.* **2021**, *262*, 118623.
(25) Wang, X.; Wang, M.; Liu, X.; Zhang, X.; Li, R. A PM2. 5 concentration estimation method based on multi-feature combination of image patches. *Environ. Res.* **2022**, *211*, 113051.
(26) Won, T.; Eo, Y. D.; Sung, H.; Chong, K. S.; Youn, J.; Lee, G. W. Particulate Matter Estimation from Public Weather Data and Closed-Circuit Television Images. *KSCE J. Civ. Eng.* **2022**, *26* (2), 865−873.
(27) Zhang, C.; Yan, J.; Li, C.; Wu, H.; Bie, R. End-to-end learning for image-based air quality level estimation. *Mach. Vis. Appl.* **2018**, *29*, 601−615.
(28) Ganji, A.; Minet, L.; Weichenthal, S.; Hatzopoulou, M. Predicting traffic-related air pollution using feature extraction from built environment images. *Environ. Sci. Technol.* **2020**, *54* (17), 10688−10699.
(29) Hong, K. Y.; Pinheiro, P. O.; Weichenthal, S. Predicting outdoor ultrafine particle number concentrations, particle size, and noise using street-level images and audio data. *Environ. Int.* **2020**, *144*, 106044.
(30) Liu, X.; Hadiatullah, H.; Khedr, M.; Zhang, X.; Schnelle-Kreis, J.; Zimmermann, R.; Adam, T. Personal exposure to various size fractions of ambient particulate matter during the heating and non-heating periods using mobile monitoring approach: A case study in Augsburg, Germany. *Atmos. Pollut. Res.* **2022**, *13*, 101483.
(31) Bendl, J.; Neukirchen, C.; Mudan, A.; Padoan, S.; Zimmermann, R.; Adam, T. Personal measurements and sampling of particulate matter in a subway-Identification of hot-spots, spatio-temporal variability and sources of pollutants. *Atmos. Environ.* **2023**, *308*, 119883.
(32) Liu, X.; Hadiatullah, H.; Zhang, X.; Hill, L. D.; White, A. H.; Schnelle-Kreis, J.; Bendl, J.; Jakobi, G.; Schloter-Hai, B.; Zimmermann, R. Analysis of mobile monitoring data from the microAeth® MA200 for measuring changes in black carbon on the roadside in Augsburg. *Atmos. Meas. Tech.* **2021**, *14*, 5139−5151.
(33) Smith, M. I.; Heather, J. P. A review of image fusion technology in 2005. *Thermosense XXVII*; SPIE, 2005; Vol. *5782*, pp 29−45.
(34) Hochreiter, S.; Schmidhuber, J. Long short-term memory. *Neural Comput.* **1997**, *9* (8), 1735−1780.
(35) Li, X.; Peng, L.; Yao, X.; Cui, S.; Hu, Y.; You, C.; Chi, T. Long short-term memory neural network for air pollutant concentration predictions: Method development and evaluation. *Environ. Pollut.* **2017**, *231*, 997−1004.
(36) Che, Z.; Purushotham, S.; Cho, K.; Sontag, D.; Liu, Y. Recurrent Neural Networks for Multivariate Time Series with Missing Values. *Sci. Rep.* **2018**, *8* (1), 6085.
(37) WHO. Billions of people still breathe unhealthy air: new WHO data. https://www.who.int/news/item/04-04-2022-billions-of-people-still-breathe-unhealthy-air-new-who-data (accessed Sept 25, 2023).
(38) Liu, X.; Hadiatullah, H.; Zhang, X.; Trechera, P.; Savadkoohi, M.; Garcia-Marlès, M.; Reche, C.; Pérez, N.; Beddows, D. C.; Salma, I.; et al. Ambient air particulate total lung deposited surface area (LDSA) levels in urban Europe. *Sci. Total Environ.* **2023**, *898*, 165466.
(39) He, J.; Gong, S.; Yu, Y.; Yu, L.; Wu, L.; Mao, H.; Song, C.; Zhao, S.; Liu, H.; Li, X.; et al. Air pollution characteristics and their relation to meteorological conditions during 2014−2015 in major Chinese cities. *Environ. Pollut.* **2017**, *223*, 484−496.
(40) Zhang, Y. Dynamic effect analysis of meteorological conditions on air pollution: A case study from Beijing. *Sci. Total Environ.* **2019**, *684*, 178−185.
(41) Liu, X.; Hadiatullah, H.; Zhang, X.; Schnelle-Kreis, J.; Zhang, X.; Lin, X.; Cao, X.; Zimmermann, R. Combined land-use and street view image model for estimating black carbon concentrations in urban areas. *Atmos. Environ.* **2021**, *265*, 118719.
(42) Athira, V.; Geetha, P.; Vinayakumar, R.; Soman, K. P. Deepairnet: Applying recurrent networks for air quality prediction. *Procedia Comput. Sci.* **2018**, *132*, 1394−1403.
(43) Wang, B.; Yan, Z.; Lu, J.; Zhang, G.; Li, T. Deep multi-task learning for air quality prediction. *Neural Information Processing: 25th International Conference, ICONIP 2018*; Springer, 2018; pp 93−103.

https://doi.org/10.1021/acs.est.3c06511
Environ. Sci. Technol. 2024, 58, 3869−3882